Research Article

Nano Research
2023, 16(5): 6670–6678

ISSN 1998-0124 CN 11-5974/O4
https://doi.org/10.1007/s12274-023-5450-3

Selective and effective oxidation of 5-hydroxymethylfurfural by tuning the intermediates adsorption on Co-Cu-CN_x

Tianyun Jing[1,§], Shaokang Yang[1,§], Yonghai Feng[1,†] (✉), Tingting Li[2], Yunpeng Zuo[3] (✉), and Dewei Rao[1] (✉)

[1] *School of Materials Science and Engineering, Jiangsu University, Zhenjiang 212013, China*
[2] *Institute of Surface Micro and Nano Materials, Xuchang University, Xuchang 461002, China*
[3] *Regional Centre of Advanced Technologies and Materials, Czech Advanced Technology and Research Institute, Palacký University, 77900 Olomouc, Czech Republic*
[†] *Present address: Pharmaceutical Sciences Laboratory and Turku Bioscience Center, Åbo Akademi University, Turku 20520, Finland*
[§] *Tianyun Jing and Shaokang Yang contributed equally to this work.*

Received: 3 November 2022 / **Revised:** 23 December 2022 / **Accepted:** 24 December 2022

ABSTRACT

Co-based catalysts are promising alternatives to precious metals for the selective and effective oxidation of 5-hydroxymethylfurfural (HMF) to the higher value-added 2,5-furandicarboxylic acid (FDCA). However, these catalysts still suffer from unsatisfactory activity and poor selectivity. A series of N-doped carbon-supported Co-based dual-metal nanoparticles (NPs) have been designed, among which the Co-$Cu_{1.4}$-CN_x exhibits enhanced HMF oxidative activity, achieving FDCA formation rates 4 times higher than that of pristine Co-CN_x, with 100% FDCA selectivity. Density functional theory (DFT) calculations evidenced that the increased electron density on Co sites induced by Cu can mediate the positive electronegativity offset to downshift the d-band center of Co-$Cu_{1.4}$-CN_x, thus reducing the energy barriers for the conversion of HMF to FDCA. Such findings will support the development of superior non-precious metal catalysts for HMF oxidation.

KEYWORDS

Co-based materials, 5-hydroxymethylfurfural (HMF) oxidative activity, 2,5-furandicarboxylic acid (FDCA) selectivity, electronegativity offset, d-band center

1 Introduction

Global energy crisis and carbon neutrality initiatives guide chemical production toward greenness and sustainability. Producing high-value-added chemicals based on biomass has sparked enormous attention, due to their sustainable, eco-friendly, and commercial potential [1, 2]. As an indispensable raw chemical, 5-hydroxymethylfurfural (HMF), a key building block for biomass conversion, can serve as the precursor for producing a variety of fine chemicals [3, 4]. The downstream products of the oxidation of HMF are high-value feedstocks, such as 2,5-furan dicarboxylic acid (FDCA), which is one of the 12 most valuable biomass-based platform chemicals identified by the U.S. Department of Energy [5–7]. At the same time, FDCA has been proved to be an ideal alternative to fossil-derived terephthalic acid (PTA) for the synthesis of environmentally friendly bio-polyesters in the production of next-generation bio-based plastics [8, 9]. Therefore, achieving the large-scale production of FDCA from the oxidation of HMF is a task of great significance.

The HMF oxidation involves complex reaction pathways and several intermediates, including 2,5-diformylfuran (DFF), 5-hydroxymethyl-2-furancarboxylic acid (HMFCA), 5-formylfurancarboxylic acid (FFCA), and FDCA, which pose a challenge in terms of catalytic efficiency [10–13]. Currently, noble metal (e.g., Pt, Pd, Ru, and Au) materials are widely used as heterogeneous catalysts with optimal catalytic performance in HMF oxidation; nevertheless, their scarcity and high-cost limit scale-up commercial applications [14–18]. In recent years, Co-based catalysts have emerged as potential alternatives for achieving high FDCA generation yield [12, 19, 20]; however, they suffer from inferior utilization of metal and reaction activity, together with a relatively low ratio of substrate/catalyst (≤ 10 mmol·g^{-1}) [8, 18, 21].

Constructing dual-metal active sites could induce long-range interaction in catalysts, as well as tunable electronic structures [22, 23]. As a result, the d-band center could be modulated by introducing a second metal site, which has a strong influence on the adsorption properties of reaction intermediates on catalysts [24–27]. Owing to strong synergistic effects, the dual-metal center holds great potential in modulating absorption energies at a near-optimal level compared to the single-metal center, thus resulting in enhanced intrinsic activity [28–30]. For instance, alloying Ni into Cu could upshift the d-band center and regulate the adsorption energies of the intermediates during the conversion of nitrate to ammonia [31]. Herein, a simple and efficient method was employed to construct Co-based dual-metal catalysts on porous N-doped carbon (CN_x) (denoted as Co-M-CN_x), through one-step pyrolysis of Co-M-Zn metal-organic framework precursors. In addition to suppressing the aggregation of the nanoparticles (NPs), the CN_x can also provide basic positively charged sites under a weakly basic environment, accelerating the dehydrogenation of aldehyde and methylol groups [32–34]. A

Address correspondence to Yonghai Feng, fengyonghai@ujs.edu.cn; Yunpeng Zuo, ypzuo01@gmail.com; Dewei Rao, dewei@ujs.edu.cn

series of Co-M-CN_x catalysts were fabricated by incorporating metals (e.g., Mn, Fe, Ni, and Cu) into the precursors. Among these catalysts, the prepared Co-$Cu_{1.4}$-CN_x displayed ultra-high utilization and activity, with FDCA formation rates of 1605 $\mu mol_{FDCA} \cdot g_{cat}^{-1} \cdot h^{-1}$, affording approximately 100% HMF conversion and 96% FDCA yield. After five cycles, the Co-$Cu_{1.4}$-CN_x catalyst maintained 99% HMF conversion and 95% FDCA selectivity. Significantly, density functional theory (DFT) calculation results indicate that the electron transfer from Cu to Co sites could induce a downshift of the d-band center through the electronegativity offset effect, which synergistically regulates the adsorption behavior of the intermediates. Such findings could provide a novel strategy to design efficient catalysts for related multi-step reactions.

2 Experimental

2.1 Chemicals

Zinc nitrate hexahydrate ($Zn(NO_3)_2 \cdot 6H_2O$), cobalt nitrate hexahydrate ($Co(NO_3)_2 \cdot 6H_2O$), copper nitrate trihydrate ($Cu(NO_3)_2 \cdot 3H_2O$), and methanol were purchased from Shanghai Chemical Reagents, China. 2-Methylimidazole was purchased from Aladdin. All reagents used were of analytical grade without further purification.

2.2 Preparation of Co-M-CN_x catalysts

The N-doped carbon-supported Co-M dual-metal catalysts were prepared by a typical procedure with modification [29]. Firstly, 5.6 mmol of $Zn(NO_3)_2 \cdot 6H_2O$, 1.8 mmol of $Co(NO_3)_2 \cdot 6H_2O$, and 0.6 mmol of $Cu(NO_3)_2 \cdot 3H_2O$ were ultrasonically dissolved in 50 mL methanol solution. Then a 100 mL uniformly dispersed methanol solution containing 64 mmol 2-methylimidazole was poured into the above solution. The mixture solution was stirred at room temperature for 24 h to obtain Co-Cu doped zeolitic imidazolate framework-8 (Co-Cu-ZIF-8). The Co-Cu-ZIF-8 precursors were collected by centrifuging and washing with ethanol three times. Next, the collected Co-Cu-ZIF-8 precursors were dried at 60 °C overnight in a vacuum oven. Finally, the precursors were pyrolyzed at 900 °C with a ramping rate of 5 °C·min^{-1} and held for 4 h in a tube furnace under an Ar atmosphere. After cooling to room temperature, the as-prepared product was denoted as Co-$Cu_{0.3}$-CN_x. For comparison, Co-$Ni_{0.3}$-CN_x, Co-$Fe_{0.3}$-CN_x, and Co-$Mn_{0.3}$-CN_x were prepared by similar processes to that of Co-$Cu_{0.3}$-CN_x except for the addition of corresponding metal salts, respectively.

2.3 Preparation of Co-Cu-CN_x catalysts

The various proportions of Co-Cu-CN_x were synthesized to optimize catalyst composition. The total amount of Co^{2+} and Cu^{2+} in the solution was 2.4 mmol. By adjusting the molar ratio of Cu^{2+}/Co^{2+}, the Co-CN_x, Co-$Cu_{0.3}$-CN_x, Co-$Cu_{0.6}$-CN_x, Co-Cu_1-CN_x, Co-$Cu_{1.4}$-CN_x, Co-Cu_2-CN_x, Co-$Cu_{3.8}$-CN_x, and Cu-CN_x were also prepared by the same experimental processes, respectively.

2.4 Catalytic test

The HMF oxidation experiment was conducted in a stainless-steel autoclave with a volume of 200 mL. Typically, 2 mmol HMF, 0.1 g catalyst, and 2 mmol Na_2CO_3 were suspended in 40 mL of deionized water and then added to the autoclave. Next, the reactor was vigorously stirred (600 rpm) and pressurized with 1 MPa O_2 at 100 °C for 12 h. After that, the catalyst was collected from the mixture solution by centrifugation and washed with deionized water, and then dried at 60 °C overnight. The catalyst was activated by annealing at 900 °C for 2 h for recycling experiments. The solution after the reaction was filtered with 0.22 μm PTFE filters and diluted 100 times to analyze the products by high-performance liquid chromatography (HPLC) equipped with an ultraviolet–visible (UV–vis) detector. 75% 5 mM H_2SO_4 and 25% methanol were used as mobile phase at 35 °C with a flow rate of 1 mL·min^{-1}. The major product and intermediates were detected at λ = 265 nm and characterized by the external standard method. The parameters of catalytic activity of HMF conversion were calculated as follows

$$\text{HMF conversion}(\%) = 1 - \frac{\text{Mole of HMF remained}}{\text{Mole of HMF introduced}} \times 100\%$$

$$\text{Selectivity}\ (\%) = \frac{\text{Mole of X in the products}}{\text{Mole of products}} \times 100\%$$
$$(\text{X} = \text{DFF, HMFCA, FFCA, and FDCA})$$

$$\text{Yield}\ (\%) = \frac{\text{Mole of X in the products}}{\text{Mole of HMF introduced}} \times 100\%$$
$$(\text{X} = \text{DFF, HMFCA, FFCA, and FDCA})$$

$$\text{FDCA formation rate}\ (\text{mol} \cdot \text{g}^{-1}\text{h}^{-1}) = \frac{\text{Micromole of FDCA formed}}{\text{Reaction time} \times \text{catalyst weight}}$$

2.5 Characterization

The transmission electron microscope (TEM) images were collected by Tecnai 12 operated at 120 kV. High-resolution transmission electron microscope (HRTEM) and energy-dispersive X-ray spectroscopy (EDS) elemental mapping images were obtained from Tecnai G2 F30 operated at 200 kV. Powder X-ray diffraction (PXRD) patterns were recorded on a Bruker D8 advanced diffractometer using Cu Kα radiation (λ = 1.5418 Å). X-ray photoelectron spectra (XPS) were conducted on a Kratos XSAM800 spectrometer using Al Kα radiation (1486.6 eV). The binding energies were calibrated according to the C 1s peak at 284.8 eV. Raman spectra were performed on Thermo Fisher DXRxi equipment with the excitation source at λ = 532 nm. Nitrogen adsorption–desorption isotherms were recorded at −196 °C on a NOVA 2000e physical adsorption apparatus. The specific surface areas and average pore size for the catalysts were measured by Brunauer–Emmett–Teller (BET) method. CO_2 temperature-programmed desorption (CO_2-TPD) was carried out using Micromeritics Auto Chem 2920 equipment with a thermal conductivity detector (TCD).

2.6 Computational methods

All first-principles calculations in this work were performed via the projected augmented wave (PAW) [35] method included in the commercial Vienna *ab-initio* simulation package (VASP) [36] based on DFT. The electron exchange-correlation was described by the generalized gradient approximation (GGA) with the function of Perdew–Burke–Ernzerhof (PBE) [37]. The energy cutoff was set to 500 eV and the *k*-meshes in the first Brillouin zones were sampled by the gamma-centered *k*-point grids 2 × 2 × 1 and 5 × 5 × 1 for structural optimization and electronic structure calculation, respectively. The vacuum gap of 15 Å was used to avoid the interaction between the periodic models. All atomic position was fully relaxed until the maximum force and energy on each atom were less than −0.04 eV/Å and 10^{-5} eV, respectively. The weak interaction has been considered through the DFT-D3 scheme [38]. To obtain the Co-Cu dual-metal model, a supercell containing 81 Co atoms and 27 Cu atoms closed with the actual

composition was constructed as the initial model by replacing Co with Cu in Co(111). Difference charge density can be defined as the charge density of the total system subtracting the charge density of two or more segments: $\Delta\rho = \rho_{AB} - \rho_A - \rho_B$, where ρ_{AB}, ρ_A, and ρ_B represent the total system, clean substrate, and adsorbed HMF species, respectively. The adsorption energy of intermediate adsorbed on the substrate can be calculated as $E_b = E_{(total)} - E_{(sub)} - E_{(int)}$, where $E_{(total)}$, $E_{(sub)}$, and $E_{(int)}$ represent the total energies of the adsorbed system, clean substrate, and HMF, or other intermediates in a vacuum, respectively. For the protonation calculation, the computational hydrogen electrode method was used to calculate the adsorption-free energies, which assumes that the chemical potential of an electron–proton pair is equal to that of $\frac{1}{2}H_2$ in the gas phase [39]. The free energies of adsorption are then calculated as $\Delta G = \Delta E + \Delta ZPE - \Delta TS$, where ΔE, ΔZPE, T, and S are adsorption energy, zero-point energy, temperature, and entropy, respectively.

3 Results and discussion

3.1 Synthesis and characterization of Co-Cu-CN$_x$

The synthetic procedure of the various Co-Cu-CN$_x$ catalysts is illustrated in Fig. S1 in the Electronic Supplementary Material (ESM). In brief, specific amounts of Co^{2+}, Cu^{2+}, and Zn^{2+} were employed as coordination sites with 2-methylimidazole to prepare Co-Cu-ZIF-8 precursors by a self-assembly step. This was followed by a carbonization treatment at 900 °C under Ar atmosphere to yield the targeted Co-Cu$_{1.4}$-CN$_x$ catalyst. In addition, the Co-CN$_x$, Cu-CN$_x$, and different Co-M-CN$_x$ (M = Mn, Fe, and Ni) catalysts were also synthesized via the proposed procedure with the corresponding coordinated metal ions (see the Experimental Section for details). This self-assembly coordination strategy can effectively suppress the excessive growth of NPs during the pyrolysis process, thus generating more active sites. After the evaporation of Zn, the porous N-doped carbon support was formed, which is highly beneficial for improving the charge/mass transfer and avoiding the aggregation of active sites of the catalyst [33, 40].

The structure of Co-Cu$_{1.4}$-CN$_x$ was characterized by various measurements, as shown in Fig. 1. The TEM images of Co-Cu$_{1.4}$-CN$_x$ reveal that Co-Cu dual-metal NPs are uniformly dispersed on the CN$_x$ support with an average size of ~ 8.9 nm in Figs. 1(a) and 1(b) and Fig. S2(a) in the ESM, mainly due to the spatial separation of Zn ions coordinated with 2-methylimidazole. The TEM images and corresponding size distribution for other Co-Cu-CN$_x$ materials (Fig. S3 in the ESM) identify that the Cu incorporation is beneficial for reducing the NP size. HRTEM images (Fig. 1(c) and Fig. S2(b) in the ESM) show obvious lattice fringes with a d-spacing of 0.207 nm, assigned to Co-Cu(111) (PDF#50-1452). The X-ray diffraction (XRD) pattern (Fig. 1(d)) shows three peaks at 44.2°, 51.5°, and 75.9°, which are well indexed to the (111), (200), and (220) planes of the Co-Cu phase, further confirming the formation of Co-Cu dual-metal NPs with crystalline alloy structure. The corresponding structural model is depicted in Fig. 1(e). The structure and composition of different Co-Cu-CN$_x$ and Co-M-CN$_x$ (M = Mn, Fe, Ni, and Cu) catalysts were characterized by PXRD . With increasing Cu ratio, the Co-Cu dual-metal gradually transforms from a homogeneous alloy phase to a bimetallic structure (Fig. S4 in the ESM). However, no diffraction peaks assigned to foreign metal NPs were observed in the Co-M dual-metal samples, indicating the formation of alloy structures (Fig. S5 in the ESM). Combined with the EDS line profile (Fig. S6 in the ESM), although the Cu intensity is much lower than that of Co, no significant boundary is observed from the Co-Cu dual-metal NPs, which demonstrates that Co and Cu homogeneously distribute in these NPs. The high-angle annular dark-field scanning transmission electron microscopy (HAADF-STEM) image (Fig. 1(f)) and the EDS elemental mapping images further confirmed the uniform distributions of C, N, Co, and Cu over the whole catalyst. EDS was also used to determine the content of Co and Cu in CoCu$_{1.4}$-CN$_x$, and the distribution result revealed that the Cu/Co atomic ratio is 1:3.4 (Table S1 in the ESM).

The basicity of the catalyst was investigated by CO_2-TPD measurements. In the TPD spectra of CN$_x$, Cu-CN$_x$, Co-CN$_x$, and Co-Cu$_{1.4}$-CN$_x$ (Fig. 1(g)), the CO_2 desorption peak of Co-Cu$_{1.4}$-CN$_x$ at around 160 °C is attributed to physical adsorption by CN$_x$, whereas the three main desorption peaks of Co-Cu$_{1.4}$-CN$_x$ at 455, 609, and 684 °C exhibit a slight positive shift relative to the peaks of Co-CN$_x$, manifesting a stronger basicity (Figs. 1(g$_1$) and 1(g$_2$)). The powerful basic sites of Co-Cu$_{1.4}$-CN$_x$ may be helpful to the dehydrogenation step during the catalysis [12, 19]. Raman spectrum of Co-Cu$_{1.4}$-CN$_x$ shows higher intensity ratio of D-band (1363 cm^{-1}) to G-band (1588 cm^{-1}) than the reference samples, suggesting the presence of more defects in the CN$_x$ support, induced by the N and metal dopants (Fig. 1(h)). Moreover, the Co-Cu$_{1.4}$-CN$_x$ catalyst exhibits a BET surface area of 622.5 $m^2 \cdot g^{-1}$ with an average pore diameter of 4 nm; and the large specific surface area favors the exposure of more active sites (Table S2 in the ESM).

To elucidate the effect of the dual-metal architecture on electronic structures and chemical states, the as-prepared Co-Cu$_{1.4}$-CN$_x$ and control samples were analyzed by XPS. The survey XPS spectra (Fig. S7 in the ESM) of Co-CN$_x$, Co-Cu$_{1.4}$-CN$_x$, and Cu-CN$_x$ indicate the coexistence of Co, Cu, N, and C elements in the final products. The Cu/Co atomic ratio in the Co-Cu$_{1.4}$-CN$_x$ catalyst was determined as 1:3.2, which is consistent with the EDS result. As shown in Fig. 2(a), the high-resolution Co 2p spectra show three pairs of peaks for Co-CN$_x$, Co-Cu$_{0.6}$-CN$_x$, Co-Cu$_{1.4}$-CN$_x$, and Co-Cu$_{3.8}$-CN$_x$, suggesting the simultaneous presence of metallic and ionic states of Co. In the Co 2p spectrum of Co-Cu$_{1.4}$-CN$_x$, the two peaks centered at 778.3 and 794.6 eV are assigned to metallic Co, while those at 780.6 and 796.4 eV are corresponded to high-valence Co-N$_x$ with a pair of satellite peaks at 785.5 and 803.2 eV [12, 22, 41]. It is worth noting that the Co 2p binding energies show small differences among the different catalysts, which can be attributed to the modulation of electronic structure by the introduction of Cu. More importantly, the Co 2p spectrum of Co-Cu$_{3.8}$-CN$_x$ shows no obvious metallic signal due to the reduced Co content. The two peaks at 779.6 and 794.6 eV are assigned to CoO$_x$ or CoC$_x$N$_y$, while those at 783.3 and 796.4 eV are corresponded to high-valence Co-N$_x$ with a pair of satellite peaks at 783.5 and 795.9 eV [42]. The high-resolution Cu 2p spectra (Fig. 2(b)) of Co-Cu$_{1.4}$-CN$_x$ display two peaks at 932.7 and 952.5 eV are assigned to Cu^0/Cu^{1+}, along with two peaks at 936 and 957.9 eV corresponding to Cu^{2+}, respectively [43]. Auger electron spectroscopy (AES) for Co-Cu$_{1.4}$-CN$_x$ (Fig. S8 in the ESM) shows an obvious Cu^0 signal along with relatively weak Cu^{1+} and Cu^{2+} peaks, indicating that Cu^0 is the dominant Cu species in the obtained product [42, 44]. Compared with Cu-CN$_x$, the clear positive shift (0.9 eV) of the Cu^0 peak in the Cu 2p$_{3/2}$ spectrum of Co-Cu$_{1.4}$-CN$_x$ echoes the negative shift of the Co^0 peak in Fig. 2(a), implying that the alloying strategy causes Co to gain electrons from Cu, which further confirms the strong electronic interactions originating from metal sites.

Moreover, the density of states (DOS) calculations for Co, Cu, and Co-Cu dual-metal were employed to examine the electronic states. Figure 2(c) suggests that Co has a higher electron density due to the electrons transfer from Cu; for compensation, the

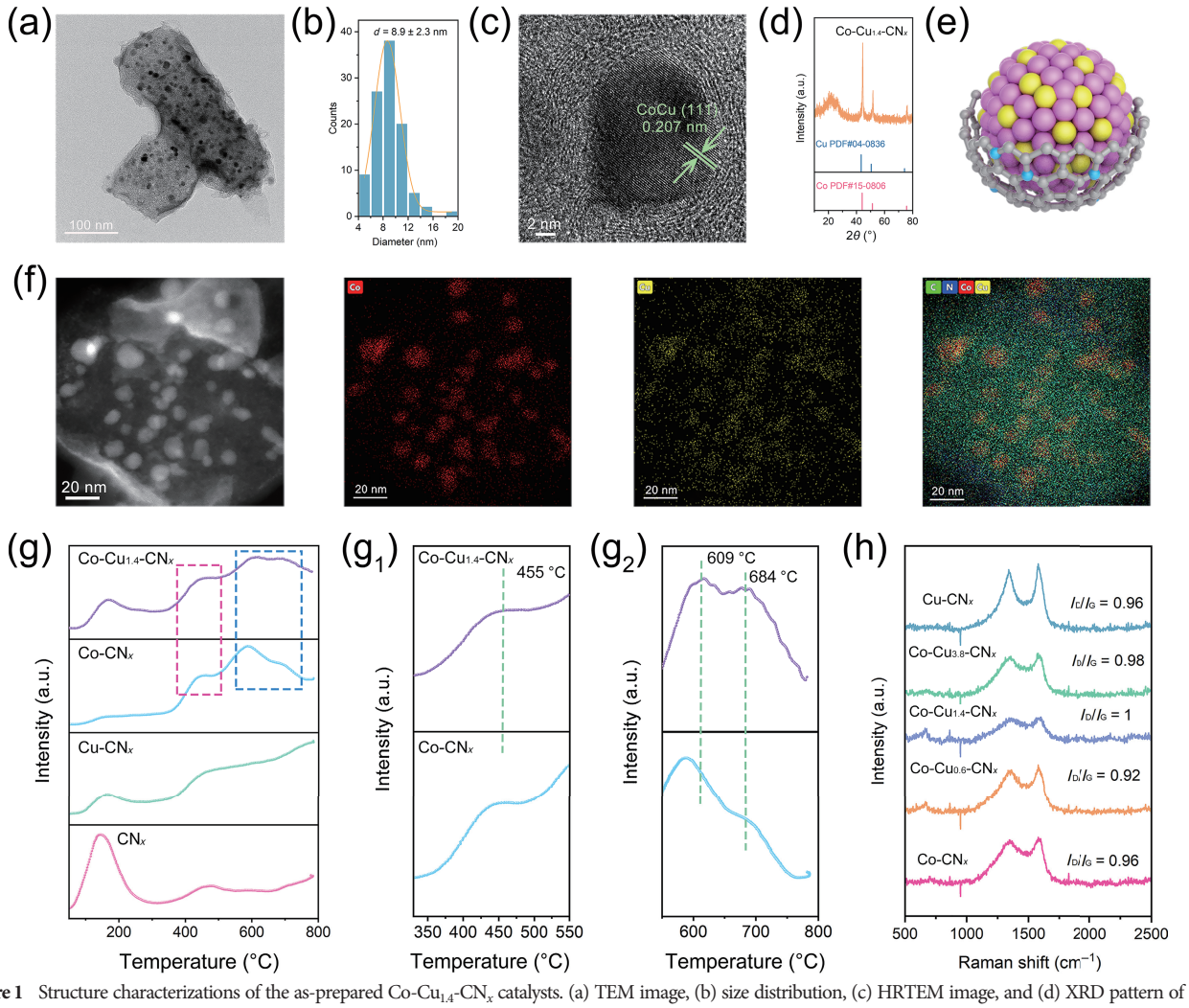

Figure 1 Structure characterizations of the as-prepared Co-$Cu_{1.4}$-CN_x catalysts. (a) TEM image, (b) size distribution, (c) HRTEM image, and (d) XRD pattern of Co-$Cu_{1.4}$-CN_x. (e) Structure model for Co-$Cu_{1.4}$-CN_x with C (gray), N (blue), Co (purple), and Cu (yellow). (f) HAADF-STEM image and corresponding element mapping images of Co-$Cu_{1.4}$-CN_x catalyst. (g) CO_2-TPD profiles for CN_x, Cu-CN_x, Co-CN_x, and Co-$Cu_{1.4}$-CN_x. (g_1) and (g_2) Enlarged profiles of Co-CN_x and Co-$Cu_{1.4}$-CN_x for the pink and blue boxes in (g). (h) Raman spectra for Co-CN_x, Co-$Cu_{0.6}$-CN_x, Co-$Cu_{1.4}$-CN_x, Co-$Cu_{3.8}$-CN_x, and Cu-CN_x.

positive electronegativity offset effect triggers a downshift of the d-band center of Co-Cu dual-metal with respect to that of pure Co, consistent with the XPS results discussed above. Figure S9 in the ESM shows the density of states for different Co-M-CN_x catalysts, which exhibits opposite electronic structure control mechanisms. The introduction of Fe could result in the downshifted d-band center of Co-Fe dual-metal, and gain electrons from Co, which is ascribed to the negative electronegativity offset. A similar result is also observed for the Co-Mn dual-metal. Conversely, although Ni alloying endowed Co with a higher electron density, an upshifted d-band center is also observed in this case. These results imply that the Co-Cu dual-metal possesses a unique electronic structure tailored by the electronegativity offset effect. The high-resolution N 1s spectrum (Fig. 2(d)) can be deconvoluted into three main peaks, and they are assigned to pyridine N, pyrrolic N, graphitic N, and oxidized N, respectively [45–47]. In addition, due to the incorporation of Cu, the N species of Co-$Cu_{1.4}$-CN_x display binding energies similar to Cu-CN_x, but lower than Co-CN_x, indicating the strong interaction between the NPs and CN_x support. The high-resolution C 1s spectrum (Fig. S10 in the ESM) can be deconvoluted into three main peaks, which are assigned to the C–C, C–O or C–N bonds, and O–C=O group, respectively [45, 46].

3.2 HMF oxidation reaction

Subsequently, the catalytic performance of the as-synthesized Co-$Cu_{1.4}$-CN_x for the aerobic oxidation of HMF was evaluated in an autoclave at 10 bar O_2 and 100 °C. Figure 3(a) shows the two possible reaction routes for the catalytic conversion of HMF to FDCA. To investigate the effect of the dual-metal elements, different Co-M-CN_x catalysts were first used to explore the relationship between metal components and activity. The product distribution reveals that the dual-metal NPs are the main active species and the introduction of Cu can effectively enhance the activity of Co NPs, achieving a higher FDCA selectivity (99%) than Co-CN_x (79%) at a small scale (Fig. S11 in the ESM). As shown in Fig. 3(b), the catalytic activity of Co-Cu-CN_x materials with different Cu/Co ratios for HMF oxidation shows a "volcano" trend, with Co-$Cu_{1.4}$-CN_x exhibiting a more favorable influence on FDCA selectivity than other Co-Cu-CN_x catalysts, which can be attributed to the synergistic effect of Co and Cu. Moreover, the effects of the experimental conditions (including O_2 pressure, temperature, reaction time, catalyst loading, HMF content, and Na_2CO_3 content) on catalytic activity were assessed to determine the optimum reaction conditions for HMF oxidation (Fig. S12 in the ESM). When the temperature was substantially increased from 60 to 120 °C in 20 °C steps, the HMF conversion showed negligible changes, while the FDCA selectivity significantly increased to 85% at 100 °C and then decreased to 67% at 120 °C (Fig. S12(a) in the ESM), revealing that this parameter plays a crucial role in improving FDCA selectivity. The O_2 pressure had a small influence on the catalytic activity: the FDCA selectivity only

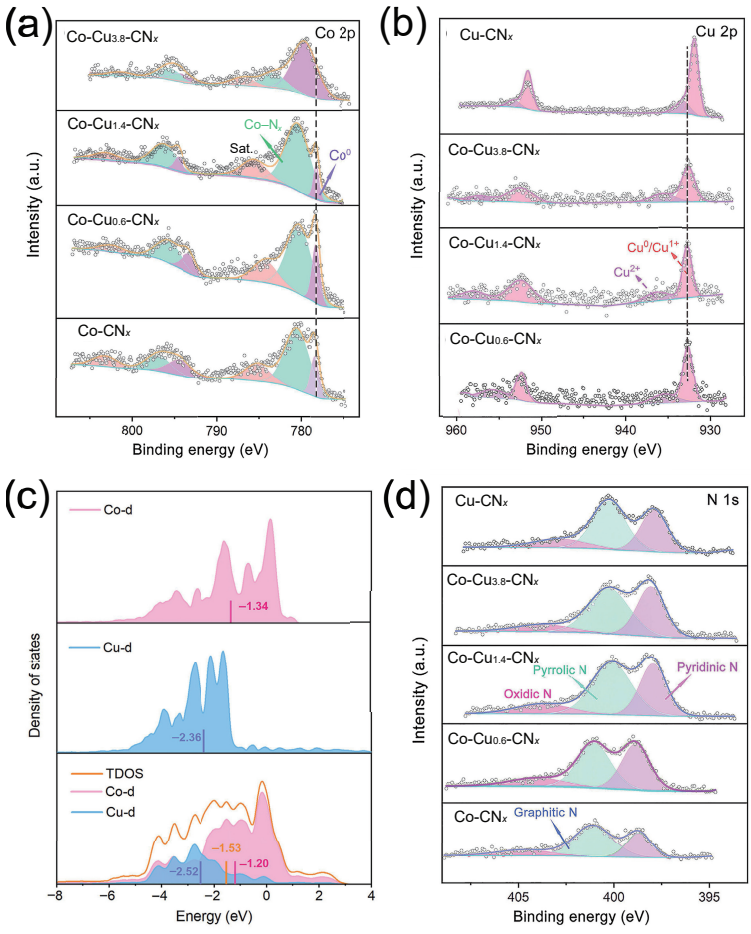

Figure 2 Electronic characterizations of Co-$Cu_{1.4}$-CN_x catalysts. High-resolution (a) Co 2p and (b) Cu 2p XPS spectra of Co-CN_x, Co-$Cu_{0.6}$-CN_x, Co-$Cu_{1.4}$-CN_x, Co-$Cu_{3.8}$-CN_x, and Cu-CN_x. (c) Density of states for the optimized structure models of Co, Cu, and Co-Cu dual-metal. (d) High-resolution N 1s XPS spectra of Co-CN_x, Co-$Cu_{0.6}$-CN_x, Co-$Cu_{1.4}$-CN_x, Co-$Cu_{3.8}$-CN_x, and Cu-CN_x.

decreased from 85% to 80% with the O_2 pressure decreasing from 10 to 1 bar, however, a decreased FDCA selectivity was observed at higher O_2 pressure (Fig. S12(b) in the ESM). Similarly, a moderate catalyst loading is essential to obtain the highest FDCA selectivity because the residual catalyst can induce undesirable side reactions (Fig. S12(c) in the ESM). Figure S12(d) in the ESM shows the time course of HMF oxidation over Co-$Cu_{1.4}$-CN_x. Only HMFCA and FFCA were detected during the catalysis, indicating that the HMF oxidation route was HMF → HMFCA → FFCA → FDCA (Fig. 3(a), route 2). Almost full conversion of HMF, together with HMFCA, FFCA, and FDCA selectivities of 9%, 32%, and 59%, respectively, were observed within 2 h. The FDCA selectivity gradually increased to 71% upon further prolonging the reaction time to 12 h, indicating that the rate-determining step (RDS) for the tandem reactions was the oxidation of FFCA to FDCA. Moreover, the Na_2CO_3/HMF molar ratio was found to play a significant role in improving the FDCA selectivity. A higher FDCA selectivity was achieved when the HMF was reduced to 1 mmol (Fig. S12(e) in the ESM) or when the Na_2CO_3 content was increased to 4 mmol (Fig. S12(f) in the ESM), entailing a Na_2CO_3/HMF molar ratio of 2. Overall, Co-$Cu_{1.4}$-CN_x could attain full HMF conversion and an FDCA yield of 96%, and no other intermediates were observed under optimal conditions, achieving much better performances than Co-CN_x (24% FDCA yield) and Cu-CN_x (2% FDCA yield) (Fig. 3(c)). This outstanding catalytic oxidation activity is superior to that of most non-noble catalysts, and even noble catalysts, delivering FDCA formation rates of 1605 $\mu mol_{FDCA} \cdot g_{cat}^{-1} \cdot h^{-1}$ at a high substrate/catalyst ratio of 20 $mmol \cdot g^{-1}$ (Fig. 3(d) and Table S3 in the ESM). The turnover frequency (TOF) and turnover number (TON) were also calculated to evaluate the intrinsic activity of Co-$Cu_{1.4}$-CN_x; the catalyst manifested high TOF and TON values of 207 h^{-1} and 8.3, respectively, toward HMF oxidation (Fig. S13 in the ESM).

Kinetic studies were conducted to further understand the intrinsic activity of the catalysts. As confirmed by previous reports and our experimental data, the oxidation of FFCA to FDCA is the RDS of the catalytic HMF oxidation [8, 13]. Kinetics experiments were carried out to reveal the influence of the dual-metal structure on the improved catalytic activity. According to the reaction order presented in Fig. S14 in the ESM, the calculated activation energy of Co-$Cu_{1.4}$-CN_x (21.2 $kJ \cdot mol^{-1}$) in the FFCA oxidation to FDCA was much lower than those of Co-CN_x (30.8 $kJ \cdot mol^{-1}$) and Cu-CN_x (59.1 $kJ \cdot mol^{-1}$) (Fig. 3(e)). In the RDS, the reaction rate for FFCA oxidation on Co-$Cu_{1.4}$-CN_x was 1.8-fold enhancements than that of Co-CN_x, while the FDCA formation rate on Co-$Cu_{1.4}$-CN_x was approximately 4-fold enhancements than that of Co-CN_x in the whole reaction process (Fig. 3(f)). These results further indicate that the dual-metal structure could accelerate the oxidation rates for each intermediate with respect to Co-CN_x and Cu-CN_x, because of the superior charge/mass transfer in the cascade reactions. Moreover, the gram scale of catalysis was also performed to confirm the outstanding performance discussed above. No obvious changes were observed in the activity and selectivity of Co-Cu1.4-CN_x under optimal conditions, reflecting its excellent catalytic activity (Fig. S15 in the ESM). The stability of the catalyst is another important indicators used to evaluate the catalytic performance. Benefiting from the protection of CN_x support, the Co-$Cu_{1.4}$-CN_x maintains excellent stability with > 99% HMF conversion, and with an almost negligible decrease in FDCA

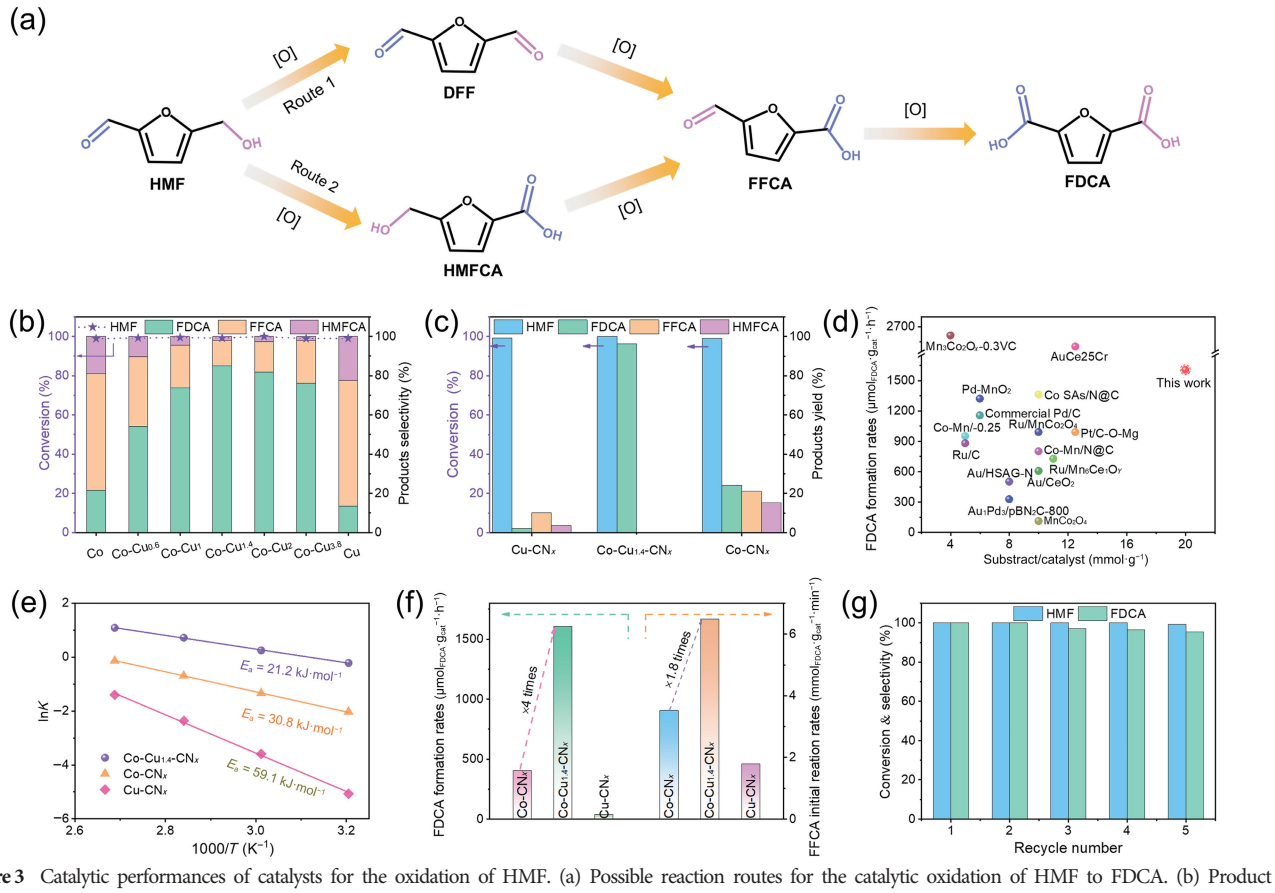

Figure 3 Catalytic performances of catalysts for the oxidation of HMF. (a) Possible reaction routes for the catalytic oxidation of HMF to FDCA. (b) Product distribution for HMF oxidation based on Co-Cu-CN_x with different Cu/Co ratios. Reaction conditions: 2 mmol HMF, 2 mmol Na_2CO_3, 100 mg catalyst, 40 mL H_2O, 100 °C, 10 bar O_2, and 12 h. (c) Catalytic performance of Cu-CN_x, Co-CN_x, and Co-$Cu_{1.4}$-CN_x under optimal reaction conditions (2 mmol HMF, 4 mmol Na_2CO_3, 100 mg catalyst, 40 mL H_2O, 100 °C, 10 bar O_2, and 12 h). (d) Comparison of substrate/catalyst ratios and FDCA formation rates of Co-$Cu_{1.4}$-CN_x and other reported catalysts. (e) Arrhenius plots for the FFCA oxidation. (f) Initial reaction rate for FFCA oxidation and overall FDCA formation rate based on Cu-CN_x, Co-CN_x, and Co-$Cu_{1.4}$-CN_x. (g) Recyclability of Co-$Cu_{1.4}$-CN_x catalyst under the reaction condition in (c). The collected Co-$Cu_{1.4}$-CN_x catalyst was reactivated under Ar atmosphere for 2 h at 900 °C before each subsequent cycle.

selectivity from 100% to 95% after five catalytic cycles (Fig. 3(g)). After the long-time stability tests, the catalysts were collected and analyzed by XRD and TEM measurements (Fig. S16 in the ESM). Notably, they maintained their pristine structure and morphology, which contributed to their superior stability.

3.3 In-depth mechanistic studies

Considering the significant differences in activity and selectivity observed for Cu-CN_x, Co-CN_x, and Co-$Cu_{1.4}$-CN_x, DFT calculations were performed to gain insight into their structure–activity relationship and catalytic mechanism of HMF oxidation. Based on the structural characterizations of Co-$Cu_{1.4}$-CN_x, the (111) plane of Co, Cu, and Co-Cu dual-metal NPs were selected as structural models (Fig. S17 in the ESM). The most stable configurations of adsorbed HMF on the optimized models are shown in Figs. 4(a)–4(c). Based on the calculated charge density difference maps, the Co-Cu dual-metal exhibited a more favorable HMF adsorption energy (−2.73 eV), whereas the adsorption on pure Co (−3.21 eV) and Cu (−1.15 eV) was too strong or too weak, respectively. The electron transfer between HMF and structural models also supported the above conclusion: a moderate amount of electron transfer was observed from HMF adsorbed on the Co-Cu dual-metal (Fig. S18 in the ESM). Combined with the analysis of electronic states and experimental data, we can infer that only the positive electronegativity offset-induced electronic structure of the Co-Cu dual-metal has great potential to improve the FDCA selectivity. The d-band center plays a significant role in determining the adsorption properties of substrate and catalyst. Therefore, the relationship between adsorption energy and d-band center position was further studied to understand the influence of the modulation of electronic configuration on catalytic activity. We determined the structures of different intermediates adsorbed on Co, Cu, and Co-Cu dual-metal (Fig. S19 in the ESM). The position of d-band center could effectively tune the adsorption strength of the reaction intermediates on the catalyst, with a nearly linear relationship (Fig. 4(d)). The Co-Cu dual-metal sites displayed more unoccupied states and weakened the adsorption of intermediates to an optimal level compared to pure Co and Cu, thus accelerating the charge transfer due to the electronegativity offset effect. This result of calculations is in good agreement with our experiments. In addition, we determined the energy barrier profiles to further understand how the HMF oxidation processes are facilitated by the Co-Cu dual-metal. The energy barrier for the RDS on Co-Cu dual-metal (35.68 kJ·mol^{-1}) is significantly lower than those of pristine Co (46.75 kJ·mol^{-1}) and Cu (38.23 kJ·mol^{-1}). The lower energy barriers for *HMFCA, *FFCA, and *FDCA on the Co-Cu dual-metal suggest that the synergistic effect of Cu and Co boosts the FDCA selectivity and the oxidation rates for the oxidation of HMF to FDCA (Fig. 4(e)).

The possible mechanism for the oxidation of HMF to FDCA is shown in Fig. 4(f). According to the results of HMF oxidation experiments, the Na_2CO_3 content plays a key role in improving the FDCA selectivity; hence, the hydrolyzed hydroxide ions may participate in the catalytic cycle [48]. In the first stage, the HMF molecules are adsorbed on Co-$Cu_{1.4}$-CN_x and interact with hydroxide ions to form geminal diols; then, they are rapidly oxidated to carboxyl groups. Subsequently, the methylol group of

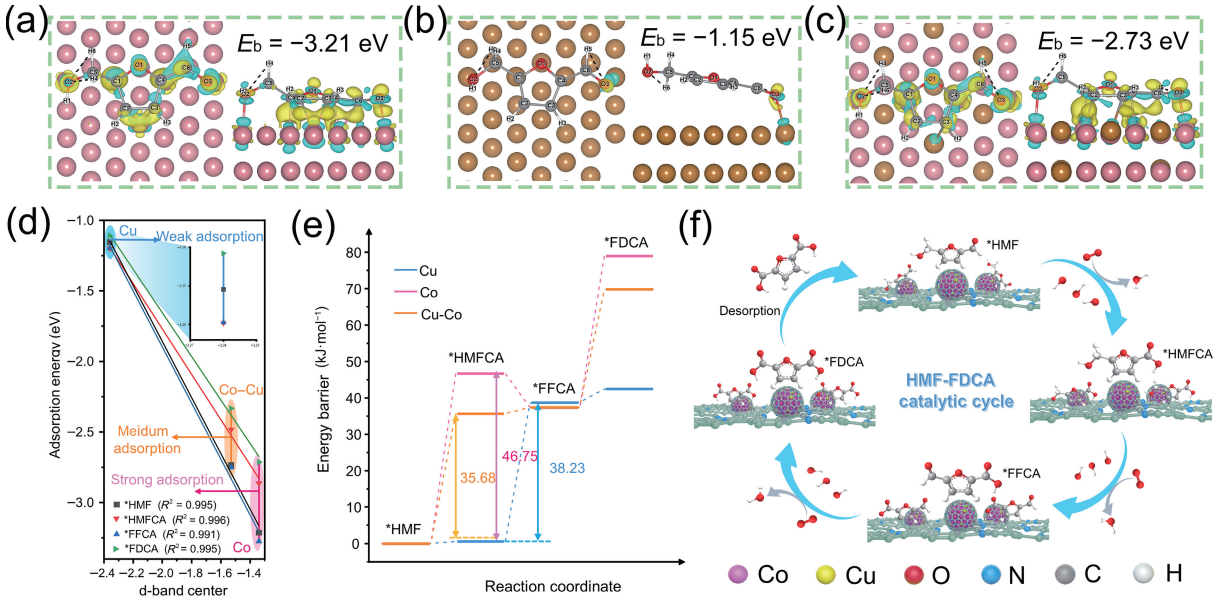

Figure 4 DFT calculations. Charge density difference maps for HMF adsorbed on (a) Co, (b) Cu, and (c) Co-Cu dual-metal based on their optimized structures. (d) Relationship between adsorption energy and d-band center for reaction intermediates and (e) energy profiles for HMF oxidation to FDCA over Co, Cu, and Co-Cu dual-metal. The pink and brown balls represent Co and Cu atoms, respectively. (f) Proposed mechanism for the selective oxidation of HMF to FDCA over Co-$Cu_{1.4}$-CN_x.

the generated HMFCA undergoes a dehydrogenation process to dissociate two protons with the aid of adsorbed hydroxide ions, along with the formation of FFCA. Finally, FDCA is produced by the oxidation of FFCA, similar to the first step. The O_2 molecule serves to regenerate the catalyst via removing the extra electrons on the catalyst surface during the catalytic cycle [49, 50]. Therefore, the adsorption energies of O_2 molecules over Co-$Cu_{1.4}$-CN_x, Co-CN_x, and Cu-CN_x catalysts were investigated by DFT calculations to elucidate the oxygen activation process. Similar to the findings obtained for the HMF and intermediates, the Co-Cu dual-metal sites show moderate adsorption strength for O_2 molecule, which may be beneficial for the HMF oxidation (Fig. S20 in the ESM).

4 Conclusions

In summary, an efficient approach was employed to fabricate Co-based dual-metal catalysts supported by porous N-doped carbon. Importantly, the synergistic effect of Cu and Co can effectively improve the FDCA selectivity. The Co-$Cu_{1.4}$-CN_x catalyst exhibits ultra-high atomic utilization and enhanced activity with approximately 100% HMF conversion and 96% FDCA yield. XPS and DFT results show that Cu sites could donate electrons to Co sites and downshift the d-band center compared to pure Co. This downshift is ascribed to the positive electronegativity offset effect that endows Co-$Cu_{1.4}$-CN_x with a unique electronic structure, thus remarkably enhancing the FDCA selectivity by modulating the intermediate adsorption and resulting in a lower energy barrier for catalytic conversion of HMF to FDCA. This work demonstrates that the electronegativity offset-mediated electronic structure is of great significance for tuning the adsorption properties for HMF oxidation, thereby providing a promising strategy to design catalysts for complex tandem reactions.

Acknowledgements

The work is supported by the National Natural Science Foundation of China (Nos. 51902281, 51801075, and 82160421), the Natural Science Foundation of Jiangsu Province (No. BK20211322), and the Scientific and Technological Projects of Henan Province (No. 212102210293).

Electronic Supplementary Material: Supplementary material (TEM images, XRD patterns, BET results, XPS spectra, and experimental and computational data) is available in the online version of this article at https://doi.org/10.1007/s12274-023-5450-3.

References

[1] Rajagopal, D.; Liu, B. The United States can generate up to 3.2 EJ of energy annually from waste. *Nat. Energy* **2020**, *5*, 18–19.

[2] Tuck, C. O.; Pérez, E.; Horváth, I. T.; Sheldon, R. A.; Poliakoff, M. Valorization of biomass: Deriving more value from waste. *Science* **2012**, *337*, 695–699.

[3] Mika, L. T.; Cséfalvay, E.; Németh, Á. Catalytic conversion of carbohydrates to initial platform chemicals: Chemistry and sustainability. *Chem. Rev.* **2018**, *118*, 505–613.

[4] Van Putten, R. J.; Van Der Waal, J. C.; De Jong, E.; Rasrendra, C. B.; Heeres, H. J.; De Vries, J. G. Hydroxymethylfurfural, a versatile platform chemical made from renewable resources. *Chem. Rev.* **2013**, *113*, 1499–1597.

[5] Lu, X. Y.; Wu, K. H.; Zhang, B. S.; Chen, J. N.; Li, F.; Su, B. J.; Yan, P. Q.; Chen, J. M.; Qi, W. Highly efficient electro-reforming of 5-hydroxymethylfurfural on vertically oriented nickel nanosheet/carbon hybrid catalysts: Structure–function relationships. *Angew. Chem., Int. Ed.* **2021**, *60*, 14528–14535.

[6] Ge, R. X.; Wang, Y.; Li, Z. Z.; Xu, M.; Xu, S. M.; Zhou, H.; Ji, K. Y.; Chen, F. G.; Zhou, J. H.; Duan, H. H. Selective electrooxidation of biomass-derived alcohols to aldehydes in a neutral medium: Promoted water dissociation over a nickel-oxide-supported ruthenium single-atom catalyst. *Angew. Chem., Int. Ed.* **2022**, *61*, e202200211.

[7] Payne, K. A. P.; Marshall, S. A.; Fisher, K.; Cliff, M. J.; Cannas, D. M.; Yan, C. Y.; Heyes, D. J.; Parker, D. A.; Larrosa, I.; Leys, D. Enzymatic carboxylation of 2-furoic acid yields 2, 5-furandicarboxylic acid (FDCA). *ACS Catal.* **2019**, *9*, 2854–2865.

[8] Liu, H.; Jia, W. L.; Yu, X.; Tang, X.; Zeng, X. H.; Sun, Y.; Lei, T. Z.; Fang, H. Y.; Li, T. Y.; Lin, L. Vitamin C-assisted synthesized Mn-Co oxides with improved oxygen vacancy concentration: Boosting lattice oxygen activity for the air-oxidation of 5-(hydroxymethyl)furfural. *ACS Catal.* **2021**, *11*, 7828–7844.

[9] Liao, Y. T.; Van Chi, N.; Ishiguro, N.; Young, A. P.; Tsung, C. K.; Wu, K. C. W. Engineering a homogeneous alloy-oxide interface derived from metal-organic frameworks for selective oxidation of 5-

hydroxymethylfurfural to 2, 5-furandicarboxylic acid. *Appl. Catal. B:Environ.* **2020**, *270*, 118805.

[10] Xu, S.; Zhou, P.; Zhang, Z. H.; Yang, C. J.; Zhang, B. G.; Deng, K. J.; Bottle, S.; Zhu, H. Y. Selective oxidation of 5-hydroxymethylfurfural to 2, 5-furandicarboxylic acid using O_2 and a photocatalyst of Co-thioporphyrazine bonded to g-C_3N_4. *J. Am. Chem. Soc.* **2017**, *139*, 14775–14782.

[11] Liu, X.; Luo, Y.; Ma, H.; Zhang, S. J.; Che, P. H.; Zhang, M. Y.; Gao, J.; Xu, J. Hydrogen-binding-initiated activation of O–H bonds on a nitrogen-doped surface for the catalytic oxidation of biomass hydroxyl compounds. *Angew. Chem., Int. Ed.* **2021**, *60*, 18103–18110.

[12] Yang, S. W.; Wu, C.; Wang, J. H.; Shen, H. D.; Zhu, K.; Zhang, X.; Cao, Y. L.; Zhang, Q. Y.; Zhang, H. P. Metal single-atom and nanoparticle double-active-site relay catalysts: Design, preparation, and application to the oxidation of 5-hydroxymethylfurfural. *ACS Catal.* **2022**, *12*, 971–981.

[13] Hayashi, E.; Yamaguchi, Y.; Kamata, K.; Tsunoda, N.; Kumagai, Y.; Oba, F.; Hara, M. Effect of MnO_2 crystal structure on aerobic oxidation of 5-hydroxymethylfurfural to 2, 5-furandicarboxylic acid. *J. Am. Chem. Soc.* **2019**, *141*, 890–900.

[14] Liao, X. M.; Hou, J. D.; Wang, Y.; Zhang, H.; Sun, Y.; Li, X. P.; Tang, S. Y.; Kato, K.; Yamauchi, M.; Jiang, Z. An active, selective, and stable manganese oxide-supported atomic Pd catalyst for aerobic oxidation of 5-hydroxymethylfurfural. *Green Chem.* **2019**, *21*, 4194–4203.

[15] Han, X. W.; Geng, L.; Guo, Y.; Jia, R.; Liu, X. H.; Zhang, Y. G.; Wang, Y. Q. Base-free aerobic oxidation of 5-hydroxymethylfurfural to 2, 5-furandicarboxylic acid over a Pt/C-O-Mg catalyst. *Green Chem.* **2016**, *18*, 1597–1604.

[16] Mishra, D. K.; Lee, H. J.; Kim, J.; Lee, H. S.; Cho, J. K.; Suh, Y. W.; Yi, Y. J.; Kim, Y. J. $MnCo_2O_4$ spinel supported ruthenium catalyst for air-oxidation of HMF to FDCA under aqueous phase and base-free conditions. *Green Chem.* **2017**, *19*, 1619–1623.

[17] Kim, M.; Su, Y. Q.; Fukuoka, A.; Hensen, E. J. M.; Nakajima, K. Aerobic oxidation of 5-(hydroxymethyl)furfural cyclic acetal enables selective furan-2, 5-dicarboxylic acid formation with CeO_2-supported gold catalyst. *Angew. Chem., Int. Ed.* **2018**, *57*, 8235–8239.

[18] Gao, T. Y.; Chen, J.; Fang, W. H.; Cao, Q.; Su, W. P.; Dumeignil, F. Ru/$Mn_xCe_1O_y$ catalysts with enhanced oxygen mobility and strong metal–support interaction: Exceptional performances in 5-hydroxymethylfurfural base-free aerobic oxidation. *J. Catal.* **2018**, *368*, 53–68.

[19] Zhou, H.; Xu, H. H.; Liu, Y. Aerobic oxidation of 5-hydroxymethylfurfural to 2, 5-furandicarboxylic acid over Co/Mn–lignin coordination complexes-derived catalysts. *Appl. Catal. B:Environ.* **2019**, *244*, 965–973.

[20] Zhou, H.; Xu, H. H.; Wang, X. K.; Liu, Y. Convergent production of 2, 5-furandicarboxylic acid from biomass and CO_2. *Green Chem.* **2019**, *21*, 2923–2927.

[21] Rao, K. T. V.; Rogers, J. L.; Souzanchi, S.; Dessbesell, L.; Ray, M. B.; Xu, C. Inexpensive but highly efficient Co-Mn mixed-oxide catalysts for selective oxidation of 5-hydroxymethylfurfural to 2, 5-furandicarboxylic acid. *ChemSusChem* **2018**, *11*, 3323–3334.

[22] Zheng, X. B.; Yang, J. R.; Xu, Z. F.; Wang, Q. S.; Wu, J. B.; Zhang, E. H.; Dou, S. X.; Sun, W. P.; Wang, D. S.; Li, Y. D. Ru-Co pair sites catalyst boosts the energetics for the oxygen evolution reaction. *Angew. Chem., Int. Ed.* **2022**, *134*, e202205946.

[23] Li, W. H.; Yang, J. R.; Wang, D. S. Long-range interactions in diatomic catalysts boosting electrocatalysis. *Angew. Chem., Int. Ed.* **2022**, *61*, e202213318.

[24] Zuo, Y. P.; Rao, D. W.; Li, S.; Li, T. T.; Zhu, G. L.; Chen, S. M.; Song, L.; Chai, Y.; Han, H. Y. Atomic vacancies control of Pd-based catalysts for enhanced electrochemical performance. *Adv. Mater.* **2018**, *30*, 1704171.

[25] Ji, Y. L.; Chen, Z.; Wei, R. L.; Yang, C.; Wang, Y. H.; Xu, J.; Zhang, H.; Guan, A. X.; Chen, J. T.; Sham, T. K. et al. Selective CO-to-acetate electroreduction via intermediate adsorption tuning on ordered Cu-Pd sites. *Nat. Catal.* **2022**, *5*, 251–258.

[26] Jiang, J. C.; Chen, J. C.; Zhao, M. D.; Yu, Q.; Wang, Y. G.; Li, J. Rational design of copper-based single-atom alloy catalysts for electrochemical CO_2 reduction. *Nano Res.* **2022**, *15*, 7116–7123.

[27] Joo, S.; Kim, K.; Kwon, O.; Oh, J.; Kim, H. J.; Zhang, L. J.; Zhou, J.; Wang, J. Q.; Jeong, H. Y.; Han, J. W. et al. Enhancing thermocatalytic activities by upshifting the d-band center of exsolved Co-Ni-Fe ternary alloy nanoparticles for the dry reforming of methane. *Angew. Chem., Int. Ed.* **2021**, *60*, 15912–15919.

[28] Lin, S. X.; Wang, Q.; Li, M. S.; Hao, Z. W.; Pan, Y. T.; Han, X. Y.; Chang, X.; Huang, S. Y.; Li, Z. H.; Ma, X. B. Ni-Zn dual sites switch the CO_2 hydrogenation selectivity via tuning of the d-band center. *ACS Catal.* **2022**, *12*, 3346–3356.

[29] Cui, T. T.; Wang, Y. P.; Ye, T.; Wu, J.; Chen, Z. Q.; Li, J.; Lei, Y. P.; Wang, D. S.; Li, Y. D. Engineering dual single-atom sites on 2D ultrathin N-doped carbon nanosheets attaining ultra-low-temperature Zinc-air battery. *Angew. Chem., Int. Ed.* **2022**, *61*, e202115219.

[30] Zhu, X. F.; Tan, X.; Wu, K. H.; Haw, S. C.; Pao, C. W.; Su, B. J.; Jiang, J. J.; Smith, S. C.; Chen, J. M.; Amal, R. et al. Intrinsic ORR activity enhancement of Pt atomic sites by engineering the d-band center via local coordination tuning. *Angew. Chem., Int. Ed.* **2021**, *60*, 21911–21917.

[31] Wang, Y. H.; Xu, A. N.; Wang, Z. Y.; Huang, L. S.; Li, J.; Li, F. W.; Wicks, J.; Luo, M. C.; Nam, D. H.; Tan, C. S. et al. Enhanced nitrate-to-ammonia activity on copper-nickel alloys via tuning of intermediate adsorption. *J. Am. Chem. Soc.* **2020**, *142*, 5702–5708.

[32] Wang, S. J.; Wang, H. Y.; Huang, C. Q.; Ye, P. C.; Luo, X. T.; Ning, J. Q.; Zhong, Y. J.; Hu, Y. Trifunctional electrocatalyst of N-doped graphitic carbon nanosheets encapsulated with CoFe alloy nanocrystals: The key roles of bimetal components and high-content graphitic-N. *Appl. Catal. B:Environ.* **2021**, *298*, 120512.

[33] Nam, G.; Park, J.; Choi, M.; Oh, P.; Park, S.; Kim, M. G.; Park, N.; Cho, J.; Lee, J. S. Carbon-coated core–shell Fe-Cu nanoparticles as highly active and durable electrocatalysts for a Zn-air battery. *ACS Nano* **2015**, *9*, 6493–6501.

[34] Donoeva, B.; Masoud, N.; De Jongh, P. E. Carbon support surface effects in the gold-catalyzed oxidation of 5-hydroxymethylfurfural. *ACS Catal.* **2017**, *7*, 4581–4591.

[35] Kresse, G.; Joubert, D. From ultrasoft pseudopotentials to the projector augmented-wave method. *Phys. Rev. B* **1999**, *59*, 1758–1775.

[36] Kresse, G.; Furthmüller, J. Efficient iterative schemes for *ab initio* total-energy calculations using a plane-wave basis set. *Phys. Rev. B* **1996**, *54*, 11169–11186.

[37] Perdew, J. P.; Burke, K.; Ernzerhof, M. Generalized gradient approximation made simple. *Phys. Rev. Lett.* **1996**, *77*, 3865–3868.

[38] Grimme, S.; Antony, J.; Ehrlich, S.; Krieg, H. A consistent and accurate *ab initio* parametrization of density functional dispersion correction (DFT-D) for the 94 elements H-Pu. *J. Chem. Phys.* **2010**, *132*, 154104.

[39] Nørskov, J. K.; Rossmeisl, J.; Logadottir, A.; Lindqvist, L.; Kitchin, J. R.; Bligaard, K. T.; Jónsson, H. Origin of the overpotential for oxygen reduction at a fuel-cell cathode. *J. Phys. Chem. B* **2004**, *108*, 17886–17892.

[40] Min, X. W.; Lv, H.; Yamauchi, Y.; Liu, B. Porous metal nanocrystal catalysts: Can crystalline porosity enable catalytic selectivity? *CCS Chem*. **2022**, *4*, 1829–1842.

[41] Zhu, G. H.; Yang, H. Y.; Jiang, Y.; Sun, Z. Q.; Li, X. P.; Yang, J. P.; Wang, H. F.; Zou, R. J.; Jiang, W.; Qiu, P. P. et al. Modulating the electronic structure of FeCo nanoparticles in N-doped mesoporous carbon for efficient oxygen reduction reaction. *Adv. Sci.* **2022**, *9*, 2200394.

[42] Liu, H.; Ding, N.; Wei, J. N.; Tang, X.; Zeng, X. H.; Sun, Y.; Lei, T. Z.; Fang, H. Y.; Li, T. Y.; Lin, L. Oxidative esterification of 5-hydroxymethylfurfural with an N-doped carbon-supported CoCu bimetallic catalyst. *ChemSusChem* **2020**, *13*, 4151–4158.

[43] Zuo, Y. P.; Rao, D. W.; Zhang, N.; Li, T. T.; Jing, T. Y.; Kment, Š.; Sofer, Z.; Chai, Y. Self-reconstruction mediates isolated Pt tailored nanoframes for highly efficient catalysis. *J. Mater. Chem. A* **2021**, *9*, 22501–22508.

[44] Zhang, Q. R.; Kumar, P.; Zhu, X. F.; Daiyan, R.; Bedford, N. M.; Wu, K. H.; Han, Z. J.; Zhang, T. R.; Amal, R.; Lu, X. Y. Electronically modified atomic sites within a multicomponent Co/Cu

composite for efficient oxygen electroreduction. *Adv. Energy Mater.* **2021**, *11*, 2100303.

[45] Yuan, S.; Zhang, J. W.; Hu, L. Y.; Li, J. N.; Li, S. W.; Gao, Y. N.; Zhang, Q. H.; Gu, L.; Yang, W. X.; Feng, X. et al. Decarboxylation-induced defects in MOF-derived single cobalt atom@carbon electrocatalysts for efficient oxygen reduction. *Angew. Chem., Int. Ed.* **2021**, *60*, 21685–21690.

[46] Yin, S. H.; Yang, J.; Han, Y.; Li, G.; Wan, L. Y.; Chen, Y. H.; Chen, C.; Qu, X. M.; Jiang, Y. X.; Sun, S. G. Construction of highly active metal-containing nanoparticles and FeCo-N_4 composite sites for the acidic oxygen reduction reaction. *Angew. Chem., Int. Ed.* **2020**, *59*, 21976–21979.

[47] Zuo, Y. P.; Li, T. T.; Zhang, N.; Jing, T. Y.; Rao, D. W.; Schmuki, P.; Kment, Š.; Zbořil, R.; Chai, Y. Spatially confined formation of single atoms in highly porous carbon nitride nanoreactors. *ACS Nano* **2021**, *15*, 7790–7798.

[48] Davis, S. E.; Zope, B. N.; Davis, R. J. On the mechanism of selective oxidation of 5-hydroxymethylfurfural to 2, 5-furandicarboxylic acid over supported Pt and Au catalysts. *Green Chem.* **2012**, *14*, 143–147.

[49] Zope, B. N.; Hibbitts, D. D.; Neurock, M.; Davis, R. J. Reactivity of the gold/water interface during selective oxidation catalysis. *Science* **2010**, *330*, 74–78.

[50] Ryu, J.; Bregante, D. T.; Howland, W. C.; Bisbey, R. P.; Kaminsky, C. J.; Surendranath, Y. Thermochemical aerobic oxidation catalysis in water can be analysed as two coupled electrochemical half-reactions. *Nat. Catal.* **2021**, *4*, 742–752.